Reduced model simulations of the scrape-off-layer heat-flux width and comparison with experiment

J. R. Myra, D. A. Russell, D. A. D'Ippolito, J.-W. Ahn, R. Maingi, R. J. Maqueda, D. P. Lundberg, D. P. Stotler, S. J. Zweben, J. Boedo, M. Umansky, and NSTX Team

---

Articles you may be interested in

Modeling the effect of lithium-induced pedestal profiles on scrape-off-layer turbulence and the heat flux width
Phys. Plasmas **22**, 092311 (2015); 10.1063/1.4930285

Simulations of drift resistive ballooning L-mode turbulence in the edge plasma of the DIII-D tokamaka)
Phys. Plasmas **20**, 055906 (2013); 10.1063/1.4804638

Boundary conditions for plasma fluid models at the magnetic presheath entrance
Phys. Plasmas **19**, 122307 (2012); 10.1063/1.4771573

The role of parallel heat transport in the relation between upstream scrape-off layer widths and target heat flux width in H-mode plasmas of the National Spherical Torus Experiment
Phys. Plasmas **15**, 122507 (2008); 10.1063/1.3043799

Edge and scrape-off layer tokamak plasma turbulence simulation using two-field fluid model
Phys. Plasmas **12**, 072520 (2005); 10.1063/1.1942427

Reduced model simulations of the scrape-off-layer heat-flux width and comparison with experiment

J. R. Myra,[1,a)] D. A. Russell,[1] D. A. D'Ippolito,[1] J.-W. Ahn,[2] R. Maingi,[2] R. J. Maqueda,[3] D. P. Lundberg,[3] D. P. Stotler,[3] S. J. Zweben,[3] J. Boedo,[4] M. Umansky,[5] and NSTX Team

[1]*Lodestar Research Corporation, Boulder, Colorado 80301, USA*
[2]*Oak Ridge National Laboratory, Oak Ridge, Tennessee 37831, USA*
[3]*Princeton Plasma Physics Laboratory, Princeton, New Jersey 08543, USA*
[4]*University of California at San Diego, La Jolla, California 92093, USA*
[5]*Lawrence Livermore National Laboratory, Livermore, California 94550, USA*

Reduced model simulations of turbulence in the edge and scrape-off-layer (SOL) region of a spherical torus or tokamak plasma are employed to address the physics of the scrape-off-layer heat-flux width. The simulation model is an electrostatic two-dimensional fluid turbulence model, applied in the plane perpendicular to the magnetic field at the outboard midplane of the torus. The model contains curvature-driven-interchange modes, sheath losses, and both perpendicular turbulent diffusive and convective (blob) transport. These transport processes compete with classical parallel transport to set the SOL width. Midplane SOL profiles of density, temperature, and parallel heat flux are obtained from the simulation and compared with experimental results from the National Spherical Torus Experiment [S. M. Kaye *et al.*, Phys. Plasmas **8**, 1977 (2001)] to study the scaling of the heat-flux width with power and plasma current. It is concluded that midplane turbulence is the main contributor to the SOL heat-flux width for the low power H-mode discharges studied, while additional physics is required to fully explain the plasma current scaling of the SOL heat-flux width observed experimentally in higher power discharges. Intermittent separatrix-spanning convective cells are found to be the main mechanism that sets the near-SOL width in the simulations. The roles of sheared flows and blob trapping versus emission are discussed. © *2011 American Institute of Physics*. [doi:10.1063/1.3526676]

I. INTRODUCTION

Diffusive and convective transport of plasma from the strong gradient region of the edge pedestal into the scrape-off-layer (SOL) sets the SOL characteristics which will be critical for future tokamak and spherical torus devices,[1] impacting power exhaust, the SOL width, density control, wall recycling, and plasma-facing component (PFC) damage. Of particular importance is the heat-flux SOL width and the resulting heat-flux density on surfaces such as divertor plates that are subject to intense plasma exhaust. The size and scaling of the heat-flux width has been the subject of recent experimental investigations,[2–6] supplementing earlier scaling studies,[7–10] and provides the main motivation for the present paper.

Heat can be transported across the separatrix by both neoclassical and turbulent processes. Notwithstanding the possibility of significant neoclassical heat transport across the separatrix (e.g., of beam ions), it is generally believed that the turbulence in the outboard midplane region dominates the cross-field transport which then competes with classical parallel transport to determine the SOL width.[7–11] The traditional theoretical approach to this problem has been to estimate a turbulent diffusion coefficient from a particular class of instabilities and then balance the cross-field diffusion

against parallel streaming.[7–9] More recent work has emphasized the importance of intermittent convective transport processes mediated by blob-filaments[12] (referred to in the future as "blobs"). It is clear that blobs can propagate far into the SOL and are important for main chamber wall recycling and possibly PFC damage. Their role, and that of associated convective cells, in setting the near-SOL width will be discussed in the present paper. Concurrent experimental investigations of the relationship of blob transport and the density SOL width are also underway.[13]

Here, using reduced model simulations with the scrape-off-layer turbulence (SOLT) code,[14] we will address the near-SOL width, including convective and diffusive processes and blob formation. SOLT code simulations will be compared with data[4,5] from the National Spherical Torus Experiment (NSTX).[15] Thus, this work complements the previous work with the SOLT code which has focused on understanding the blob velocity in the far SOL and in testing the present theoretical and simulation models with the experimental data obtained from gas puff imaging (GPI) experiments on NSTX.[16–18]

The physics model described by the SOLT code is relatively simple, yet still very rich. It describes $\mathbf{E} \times \mathbf{B}$ turbulence by filamentary (interchange-like) fluctuations in the two-dimensional plane perpendicular to the local magnetic field. An overview of the physics model is described in Sec. II. Similar models have been successfully employed by

a)Electronic mail: jrmyra@lodestar.com.

other authors to study blob dynamics and the width and characteristics of the SOL plasma in tokamaks.[19–22] Theoretical investigations in simpler toroidal geometries have also employed similar physics models.[23]

The present work extends previous investigations in several respects. Most significant is the focus on the scaling of the heat-flux width, and the comparison of simulation results with experimental data. Comparisons are reported here for the midplane-mapped heat-flux width, midplane SOL plasma profiles, and midplane GPI using a synthetic GPI diagnostic in SOLT. Questions addressed include the size and scaling of the SOL width, and the role of diffusion, convective cells, and blobs.

The primary issue addressed here is determining whether midplane-region electrostatic turbulence is the dominant cross-field transport mechanism determining the SOL width. We will answer this question in the affirmative for one case, and in the negative for another. The model employed, being a two-dimensional fluid model, is not precise enough to expect better than factor-of-two agreement in an absolute sense. But comparison of trends and understanding the physics mechanisms responsible for them is a reasonable and important goal. An overview containing some of the results presented here was given previously in a short conference paper.[24] The present paper expands and extends the previous exposition.

II. SIMULATION MODEL

A. SOLT code physics model

SOLT is a two-dimensional (2D) electrostatic fluid turbulence code. The code models the evolution of vorticity, density, temperature, and mean fluid momentum in the plane perpendicular to the magnetic field **B**, here taken as the outboard midplane of the torus. SOLT contains a reduced description of the electron drift wave and interchange instabilities, and sheath physics. Curvature- and grad-B-driven charge polarization enable blob transport of strong fluctuations ($\delta n/n \sim 1$) from the edge into the SOL. The parallel physics is modeled by closure schemes which depend upon the regime. Detailed descriptions of the SOLT code have been given in previous publications.[14] Here, we present a brief summary of the equations that are solved. The code has recently been generalized to allow regime-dependent closures for the parallel current and heat flux. These are discussed in Appendix A.

The basic equations of the SOLT model in dimensionless form (using the Bohm normalization with time-scale $\Omega_{ci} = ZeB/m_ic$ and space scale $\rho_{sr}=c_{sr}/\Omega_{ci}$, where $c_{sr}^2=T_{er}/m_i$ and T_{er} is a reference temperature for the normalization) are

$$\frac{\partial}{\partial t}\nabla^2\widetilde{\Phi} + \{\mathbf{v}\cdot\nabla\nabla^2\Phi\}$$

$$= \left\{ \alpha_{dw}\frac{\overline{T}^{3/2}}{\overline{n}}(\Phi - T\ln n) + \alpha_{sheath}\frac{J_\parallel}{n} - \frac{\beta}{n}\frac{\partial(nT)}{\partial y} + \mu\nabla^4\Phi \right\}, \quad (1)$$

$$\frac{dn}{dt} = \alpha_{dw}\overline{T}^{3/2}\{\Phi - T\ln n\} - \alpha_{sheath}(nT^{1/2} - J_\parallel)$$
$$+ D\nabla^2 n + S_n, \quad (2)$$

$$\frac{dT}{dt} = -\alpha_{sheath}\frac{q_\parallel}{n} + S_T, \quad (3)$$

$$\frac{\partial p_y}{\partial t} + \frac{\partial}{\partial x}\langle nv_xv_y\rangle = -\int_x^{L_x}dx\,\alpha_{sheath}\langle J_\parallel\rangle + \overline{\mu}\frac{\partial^2}{\partial x^2}\overline{v}_y. \quad (4)$$

The simulation plane is denoted as the (x, y) plane, where x is the radial direction and y is binormal (approximately poloidal). Here, for any quantity Q, $\langle Q\rangle \equiv \overline{Q}$ denotes the zonal or y average part and $\widetilde{Q} \equiv \{Q\} \equiv Q - \overline{Q}$ denotes the fluctuating part, $\mathbf{v} = \mathbf{e}_z \times \nabla\Phi$ and $d/dt = \partial/\partial t + \mathbf{v}\cdot\nabla$. These equations evolve fluctuating vorticity $\nabla_\perp^2\widetilde{\Phi}$, plasma density n, electron temperature T, and zonally averaged momentum $p_y = \langle nv_y\rangle$, where $v_y = \partial\Phi/\partial x$. The fluctuating and zonally averaged potential $\widetilde{\Phi}$ and $\overline{\Phi}$ can then be extracted. The integral in Eq. (4) extends to the end of the simulation box $x = L_x$ and describes the dissipation of momentum in the sheaths. A derivation and further discussion of these equations is given in previous work.[14] Input parameters and profiles are discussed subsequently.

To close the system of equations, the parallel current and heat flux $J_\parallel$, $q_\parallel$ must be expressed in terms of the dynamic variables Φ, n, and T. A new and recently implemented set of closure relations, valid for a range of collisionality regimes from conduction-limited to sheath-connected, is discussed in Appendix A. The low collisionality limit of the expressions in Appendix A recovers the sheath-connected limit used in previous work.[14]

The most important input parameters of the model for the present application are

$$\alpha_{sheath} = \frac{\delta_{geo}\rho_{sr}}{L_\parallel} \quad (5)$$

and

$$\beta = \frac{2\rho_{sr}}{R}. \quad (6)$$

α_{sheath} specifies the sheath losses in terms of the connection length $L_\parallel$ and a geometrical factor $\delta_{geo}=1$ in the present work. (For asymmetrical sheaths, such as in single null geometry, $L_\parallel$ is the distance to the nearest divertor, and the divertor sheath connection the long way around is ignored. In the symmetrical case, $\delta_{geo}=2$ to describe faster end losses when both ends are effective as charge sinks.) For the shots simulated in this paper, α_{sheath} and $L_\parallel$ are taken from actual NSTX shot geometry. The parameter β provides the curvature drive for interchange instability, where R is the radius of curvature, approximately the major radius of the torus at the outboard midplane.

Additional, less important, parameters for the present work are α_{dw}, which is an adiabaticity parameter for the model drift-wave term.[14] It is small in the present runs. Also, μ, $\overline{\mu}$, and D are dissipation parameters. Here, we set D=0

and $\bar{\mu}=0.01$ (which is essentially negligible). The viscosity parameter μ is fixed for each set of runs and is given in Secs. III and V together with α_{sheath}, β and the reference values for the Bohm normalization. The dissipation parameters influence the level of turbulence through damping of both fluctuations and of zonal flows.[14]

Density and temperature sources and sinks are given by the functions S_n and S_T. They sustain quasisteady profiles in the face of turbulent losses in the SOL. Their detailed form is given in Ref. 14; however, as will be apparent shortly these details are not very important in the present application where the goal is a good description of the SOL. In the SOL, $S_n=S_T=0$.

Postprocessing tools used with the SOLT code implement many diagnostics. Among these is synthetic GPI, which is of special interest in the present paper. In GPI, a gas, typically He or D, is puffed into the plasma from an edge manifold at a specific toroidal and poloidal location, here near the outboard midplane. When the neutrals that comprise the puffed gas experience electron collisions, line radiation is emitted. The intensity of radiation takes the form

$$I_{gpi} = n_0 f(n_e, T_e), \qquad (7)$$

where n_0 is the neutral density of the puffed gas, and $f(n_e, T_e)$ is a known function that depends on atomic physics. In the experiments simulated here, the puffed gas is deuterium and the radiation of interest comes from the D_α line.

Since turbulent values of n_e and T_e are available on the spatial x-y grid for each simulation time step, once n_0 is known it is straightforward in principle to generate the radiation pattern coming from filamentary structures (which depend approximately on only x and y). This synthetic GPI data mimics that collected by the GPI cameras on NSTX.[25,26] The main complication comes from the fact that n_0 is not measured directly. Calculation of n_0 requires treatment of neutral transport, molecular and ionization physics, and has been carried out in some cases using Monte Carlo simulations with the DEGAS-2 code.[27] Here, we rely on an approximate procedure for obtaining n_0 which employs a sophisticated fitting procedure to a set of DEGAS runs. This procedure is described in Appendix B. Consistent with earlier studies, we assume in the synthetic GPI modeling that $n_0(x)$ is approximately independent of both y and t on the time scales of interest for turbulence.[27] (There is a weak decrease of n_0 with y, as distance from the manifold increases.)

B. SOL width simulation technique

With source functions S_n and S_T that yield approximately tanh-like density and temperature profiles near the edge (i.e., closed surface region), and a simulation box that encompasses the edge gradient region and the SOL, we have successfully carried out several physics studies of the turbulent edge, and modeled low-confinement-mode (L-mode) discharges in NSTX.[14,17,18,28] Such simulations describe the growth and saturation of blob-forming interchange turbulence, which is regulated by the self-consistent generation of sheared zonal flows $\langle v_y(x)\rangle$ by Reynolds stress, blob emis-
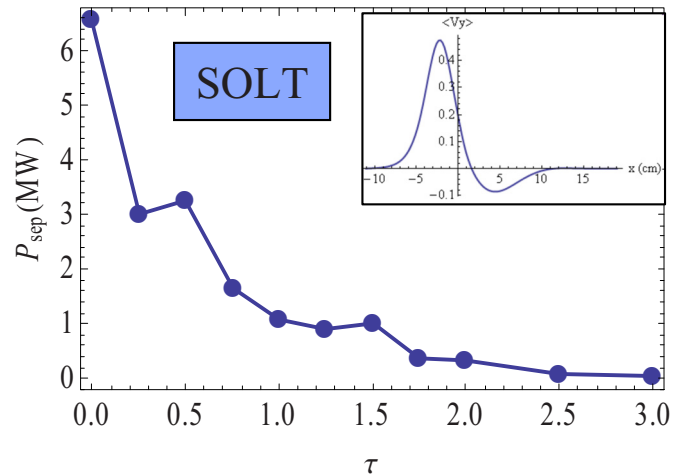

FIG. 1. (Color online) Variation of power crossing the separatrix in SOLT code simulations for various levels of mean flow imposed in the core. The mean flow control parameter is τ (see text). Inset: typical radial profile of the mean flow $\langle vy \rangle$ which is proportional to the negative of the radial electric field, E_r. Note the E_r well.

sion, and sheaths. Here, we have a somewhat different goal: to simulate the SOL of high-confinement-mode (H-mode) discharges.

In H-mode, the plasma gradients are much steeper than in L-mode discharges, yet the turbulence is weaker. It is widely believed that mean $\mathbf{E}\times\mathbf{B}$ flows arising from a "well" structure in $E_r(x)$ play a role in the suppression of turbulence.[29–32] This well structure is inside the last closed flux surface (LCFS), and affects the flux of particles and energy across the separatrix, but not directly the turbulent dynamics in the SOL. In the present work, *inside the LCFS* we enforce relaxation of the zonal flows $\langle v_y(x)\rangle$ to a specified profile, chosen here to take the form

$$v_y = -E_x = -\frac{\tau}{n}\frac{d}{dx}(nT_e), \qquad (8)$$

where the constant τ is regarded as a control parameter that is varied, as discussed subsequently. (In the SOL, only first principles physics, e.g., Reynolds stress, blob emission, and sheaths, governs $\langle v_y(x)\rangle$.) We note parenthetically that setting $\tau=T_i/T_e$ forces balancing of the $\mathbf{E}\times\mathbf{B}$ and ion diamagnetic flow, which is the observed radial force balance in H-mode pedestals,[33] so we expect τ to be an order-unity parameter.

In SOLT simulations, we find that τ functions as a very effective control parameter for the heat flux crossing the separatrix, defined as

$$P_{sep} = \int dA \cdot q_\perp = 2\pi R b_\theta \int dr q_\|, \qquad (9)$$

where $b_\theta = B_\theta/B$, the last form uses $\nabla\cdot\mathbf{q}=0$ (no heat sources in the SOL), and $\nabla_\| q_\| = (1/\nu R)(\partial q_\|/\partial\theta)$ with the local safety factor defined as $\nu = rB/RB_\theta$. Results of a typical τ scan are illustrated in Fig. 1. As τ is increased, the mean sheared flow in the steep density gradient region increases (i.e., the E_r well
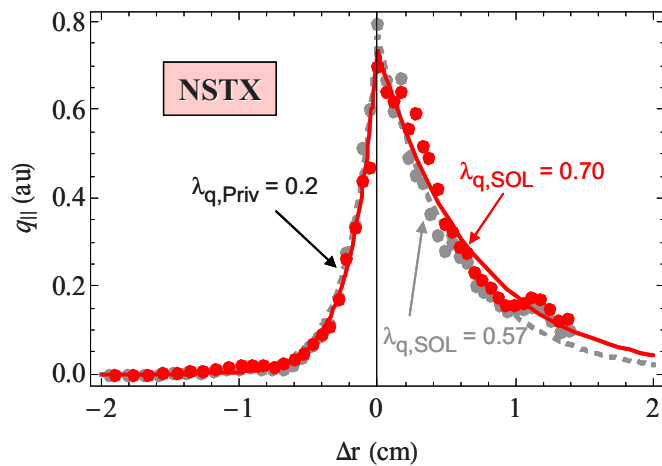
FIG. 2. (Color online) NSTX experimental heat flux, mapped to the outboard midplane for shots 135009 (gray $\lambda_{qSOL}=0.57$ cm) and 135038 (red/black $\lambda_{qSOL}=0.70$ cm). Data from the IRTV are shown as dots, exponential fits are shown as solid lines.

is deepened), causing a reduction in the turbulence level. Weaker turbulence results in smaller turbulent fluxes, and hence a reduction in P_{sep}. Thus, by choosing the value of τ that makes P_{sep} attain the experimental value of power (crossing the separatrix) for the given set of conditions, we effectively enforce a heat-flux-driven boundary condition at the separatrix for our SOL simulation.

The treatment of the source functions S_n and S_T in these H-mode simulations requires further discussion. Since our goal here is simulation of the SOL, where $S_n=S_T=0$ (i.e., the SOL is fueled entirely by transport from the edge plasma), sources are only required to maintain the profiles somewhere inside the LCFS. Here, we configure the sources to maintain the experimental measured profiles for n and T in the steep pedestal region. These artificial sources are set to zero for $r > r_{sep} - \Delta$, where we typically choose $\Delta \sim 1$ cm (comparable to the size of local turbulent structures). Having Δ non-zero allows the simulation to adjust the values of n and T on the separatrix to whatever is consistent with the turbulence.

Simulations reported here are initialized with smooth density and temperature reference profiles upon which small random seed fluctuations are superimposed. The simulations are run for at least twice the time it takes to establish a turbulent steady-state. Only the last half of the simulation is analyzed to obtain the average SOL profiles reported here.

Several other simulation details deserve mention. First, SOLT code P_{sep} power scans presented throughout this paper are actually τ scans. In a SOLT power (τ) scan, all other parameters, and in particular S_n and S_T, are held fixed. This may differ from an experimental power scan in which the pedestal parameters would likely vary. Second, in the applications discussed in this paper, the parallel current closure regime is essentially sheath-connected (i.e., the low collisionality limit of the closures in Appendix A). Finally, most of the simulations have been performed on a 128×128 spatial grid using a box size of approximately 30 cm $\times$ 30 cm. The domain in x is much larger than the typical SOL width to ensure that no unphysical interactions occur at the simulation boundaries—the sheaths damp all fluctuations (i.e.,
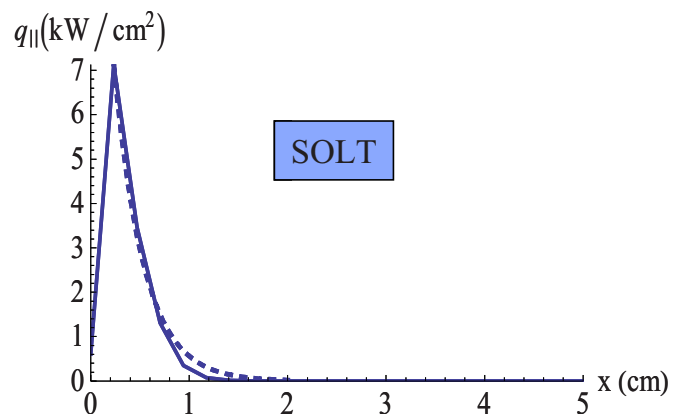
propagating blobs or holes) to zero before they encounter a wall. Separate runs with double the resolution, and double the box size in y, were carried out with little change in results (see Sec. V and Fig. 11). Finally, since both experimental and simulation data are discussed in this paper, and it is critical to avoid confusion, all simulation figures will be labeled with "SOLT" (blue) while NSTX experimental data are labeled "NSTX" (red).

III. LOW POWER ELM-FREE H-MODE AND POWER SCALING

The first set of experiments that were modeled was a set of Edge Localized Mode (ELM)-free H-modes on NSTX with low power neutral beam heating levels $P_{nb}=0.8$ MW (shot 135009) and $P_{nb}=1.3$ MW (shot 135038). A full description of the experiments is presented elsewhere.[6] These experiments were conducted in a lithium-wall environment, which enabled the suppression of ELMs. A heat flux measurement using infrared thermography (IRTV) was per-

FIG. 3. (Color online) SOLT simulation of the midplane parallel heat flux for shot 135009 (solid) and exponential fit (dashed).
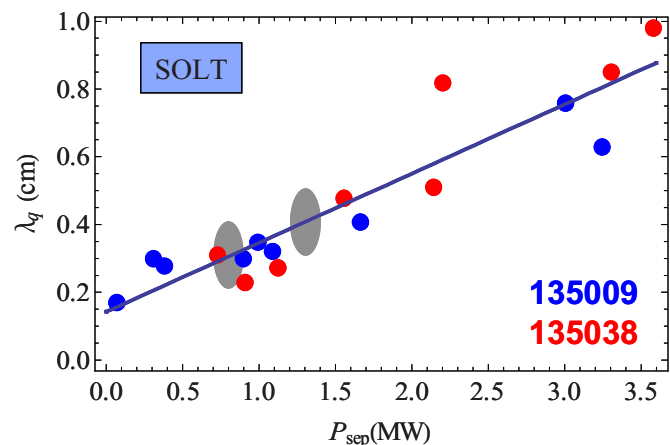

FIG. 4. (Color online) Heat-flux width for simulated power scans for shots 135009 and 135038. The code inputs for these shots are nearly the same, so they are essentially indistinguishable in the plot. The solid line is a linear fit to the code data for both shots. Gray ellipses mark the actual experimental power levels for these two shots. Reprinted from Ref. 24, J. R. Myra, D. A. Russell, D. A. D'Ippolito, J.-W. Ahn, R. Maingi, R. J. Maqueda, D. P. Lundberg, D. P. Stotler, S. J. Zweben, and M. Umansky, J. Nucl. Mater. (in press), with permission from Elsevier.

TABLE I. Power scaling of the SOL width for low power ELM-free H-modes. The first six columns, described in the text, are from the experiment. The last column is the midplane SOL width from the SOLT simulations.

Shot	P (MW)	$\lambda_{q,SOL}$ (cm)	$\lambda_{q,priv}$ (cm)	λ_{q1} (cm)	λ_{q2} (cm)	$\lambda_{q,SOLT}$ (cm)
135009	0.8	0.57	0.21	0.36	0.52	0.30
135038	1.3	0.70	0.20	0.50	0.67	0.41

formed at the divertor and flux-mapped to the outboard mid-plane. Results for the two shots are shown in Fig. 2 together with corresponding exponential fits for the heat-flux width on both the private SOL ($\Delta r < 0$) and main SOL ($\Delta r > 0$) sides of the strike point. Note the spreading of the heat flux into the private SOL region, which is a likely indication of plasma transport between the X-point and divertor plate. However, broadening on the main SOL side is stronger and shows a weak power dependence.

A typical SOLT code result for the radial variation of the heat flux is shown in Fig. 3 for $P_{sep} = 0.86$ MW. The radial profile is given versus x ($\equiv \Delta r$) measured from the location of the LCFS. This case is one of the runs for shot 135009 to be discussed in connection with Fig. 4. The main point to notice is that $q_{\parallel}$ displays nearly exponential decay into the SOL. For the grid-point exactly on the separatrix at x=0, the code enforces $q_{\parallel} = 0$.

SOLT simulation power (i.e., τ) scans were carried out for both shots, and results are shown in Fig. 4. For all the runs in Secs. III and IV, the dimensionless parameters are $\mu = 0.1$, $\beta = 8.0 \times 10^{-3}$, and $\alpha_{sheath} = \rho_{sr}/(a_f + b_f \log[x(cm)])$, where the connection length $L_{\parallel}$ in the denominator was fit from an equilibrium reconstruction with $a_f = 750$ cm and $b_f = -225$ cm. The reference values for the Bohm normalization are $T_{er} = 125$ eV, $\rho_{sr} = 0.60$ cm. The code inputs for these shots are nearly the same (there are slight but not very significant differences in the profiles inside the LCFS), so in terms of applying simulations to model the data, the only significant difference is the power level itself. In the figure, gray ellipses mark the actual experimental power levels for these two shots. The linear fit to the combined simulation data (for both shots) gives the simulation scaling of λ_q with P_{sep}. At the P_{sep} power levels corresponding to the actual experimental conditions, we obtain the (linear fit) values for λ_q.

Results from the SOLT power scan are summarized in Table I together with the midplane-mapped experimental results for λ_q. As previously mentioned, the SOLT modeling is expected to account for that portion of the heat-flux width due to main SOL turbulent transport in the outboard midplane region, but not any additional transport that might be present between the X-point and the plate. To account for this extra diffusion heuristically, as well as any heat diffusion on the divertor plate itself that might affect the measurement of $q_{\parallel}$, Table I displays the difference between the measured λ_q on the main SOL side and private flux regions, i.e., $\lambda_{q1} = \lambda_{qSOL} - \lambda_{qpriv}$. In some strictly diffusion-based models, a quadrature subtraction, denoted $\lambda_{q2} = (\lambda_{qSOL}^2 - \lambda_{qpriv}^2)^{1/2}$, may
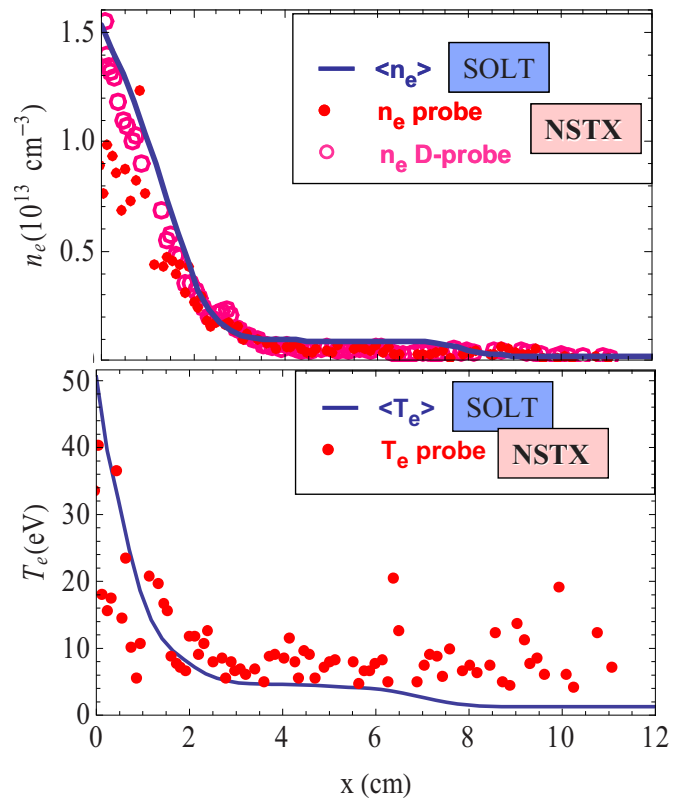

FIG. 5. (Color online) Midplane plasma profiles in the SOL for shot 135009. Points indicate experimental data, solid lines are the time and zonally averaged simulation results.

provide a better correction.[34] In any case, both simulation and experiment show a weak positive scaling of λ_q with power.

An important feature of the experimental data set for these low power shots is the availability of plasma profiles from the midplane reciprocating probe.[35] These data allow direct comparison with quantities calculated by the SOLT simulations. Note that in the simulations the SOL density profile arises entirely from turbulent transport, and does not use any direct experimental profile inputs in the SOL itself. A comparison of average profiles for shot 135009 is shown in Fig. 5. The comparison for shot 135038 is similar. For the density, results from two probe pins are shown: the single receded Mach probe (labeled "probe," filled circles) and protruding double probe (labeled "D-probe," open circles). (See Ref. 35 for a detailed description of the probes.)

As seen from the figure, the simulations provide a reasonable match to the experimental data, and support the case that the present physics model describes the cross-field turbulent transport that sets the midplane density and temperature SOL width. This lends support to the previous assertion that midplane turbulence is the dominant mechanism setting the heat-flux width at the divertor in these shots. The possibly significant discrepancy for T_e in the far SOL may be due to inaccuracies in the modeled $L_{\parallel}$ (magnetic reconstructions were not available at this location) or it may be due to difficulty in making accurate probe measurements because of the small signal-to-noise ratio.

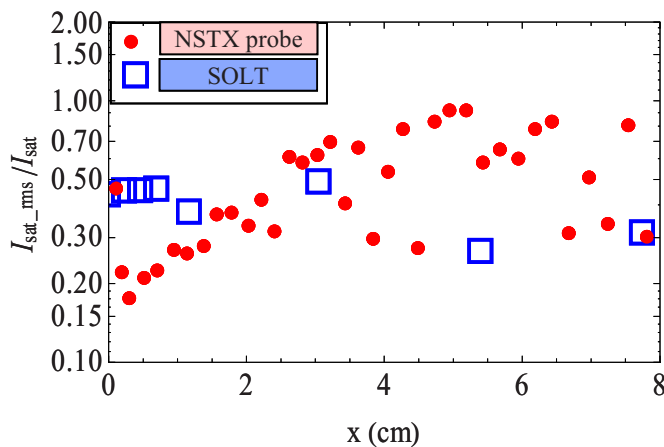In addition to average profile data from the probes, we

FIG. 6. (Color online) Measured and simulated fluctuation levels at the midplane vs radial distance from the separatrix for shot 135009.

FIG. 8. (Color online) Snapshots from SOLT simulations using synthetic GPI. Emission of a blob (circled) occurs in frames at (a) 0 μs, (b) 12 μs, and (c) 29 μs. Times are relative to frame (a) and the blob emission is triggered by the initial transient. Frame (d) is typical of the quasisteady-state after 1.5 ms of simulation. The palette denotes synthetic GPI intensity.

can validate the simulation of the midplane turbulence itself from the fluctuation data for the probe saturation current I_{sat}. Figure 6 shows the comparison of the normalized rms fluctuation level $\delta I_{sat}/\langle I_{sat}\rangle$ from a protruding biased probe[35] and the simulation. In the simulation, I_{sat} was synthesized as $I_{sat} \propto n_e (2T_e)^{1/2}$. Within scatter, the results are in broad agreement. NSTX data tend to show an increasing normalized fluctuation level going into the far SOL, while in SOLT it tends to decrease for these H-mode simulations. This may be related to the lack of blob emission in these simulations, as discussed Sec. IV. Alternatively, a finite noise floor in the probe data tends to artificially increase $\delta I_{sat}/\langle I_{sat}\rangle$ in the far SOL.

IV. SOL WIDTH MECHANISMS

Having demonstrated that turbulence at the outboard midplane region is the plausible cause of the observed heat-flux width at the divertor plates, it is of interest to examine in more detail the mechanism for the turbulence-induced cross-field transport. We demonstrate in this section, using SOLT code results consistent with NSTX GPI data, that the mechanism is intermittent separatrix-spanning convection.

Figure 7 shows a snapshot of the turbulent density field in color shades, on top of which is superimposed some contours of electrostatic potential, giving the stream lines for the $\mathbf{E}\times\mathbf{B}$ flow. The potential shows an up-down flow pattern that is sheared from left to right. The flow pattern has embedded within it closed vortex structures (island convective cells) that can transport plasma radially. In the figure, finger-like structures (arrowed) have been ejected from the main plasma, but in the presence of the strong H-mode sheared flow, these structures cannot penetrate far radially into the SOL. Rather they are sheared downward by the flow. Intermittently, the extra plasma gets carried across the LCFS by the convective cells. The resulting cross-field motion competes with parallel flow to establish the SOL width.

In weaker flow cases, the flow would shear (effectively cut) these fingers into isolated blob structures, which is what occurs in L-mode simulations. This dynamics of blob formation has been reported elsewhere.[14,36,37]

Thus, in the present H-mode simulations, blob emission does not play a significant role in setting the near-SOL width. In the SOLT simulation for this shot, in fact, blob emission only occurs due to transients at the start of the simulation.
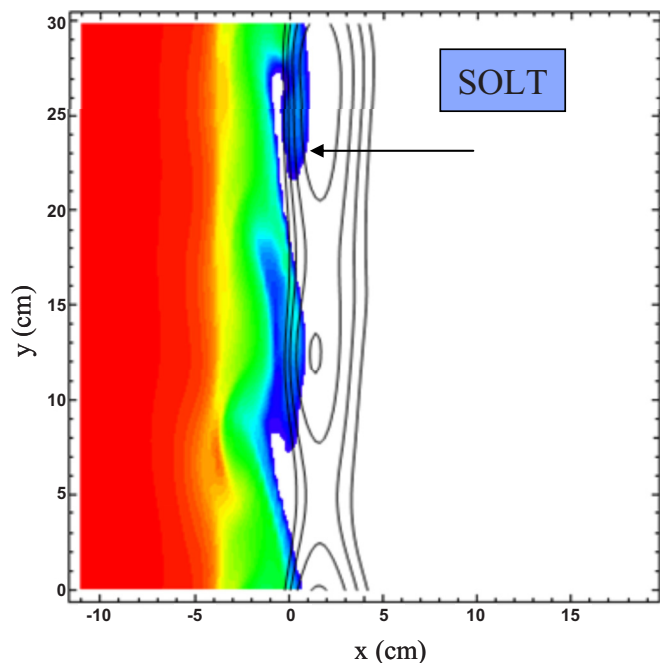

FIG. 7. (Color online) Mechanism for setting of the near-SOL width by intermittent separatrix-spanning convection. Shown is a snapshot of the turbulent fields of density (logarithmic color palette, which is truncated to white for $n/n_{ped} < 0.3$) and potential (contours shown are for $e\Phi/T_{eref} = 0.7$, 0.8, 0.9, and 1.0). The arrow points to a downward-sheared finger structure (see text).
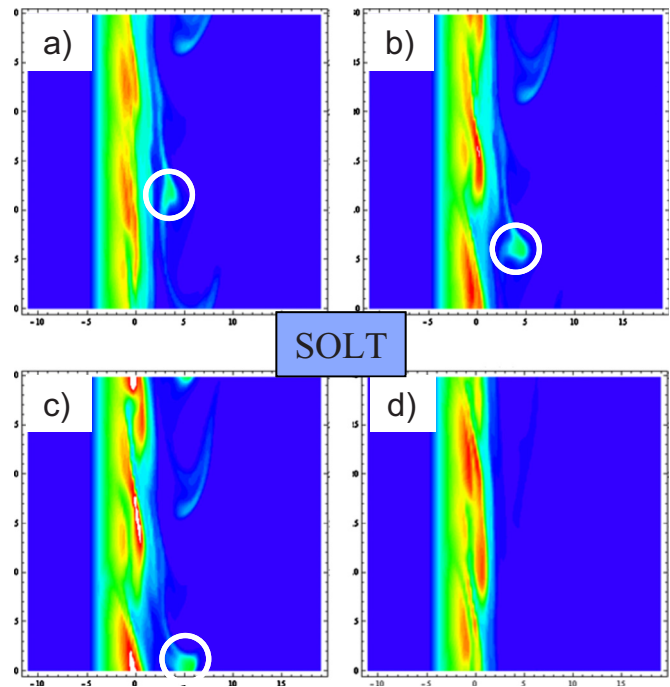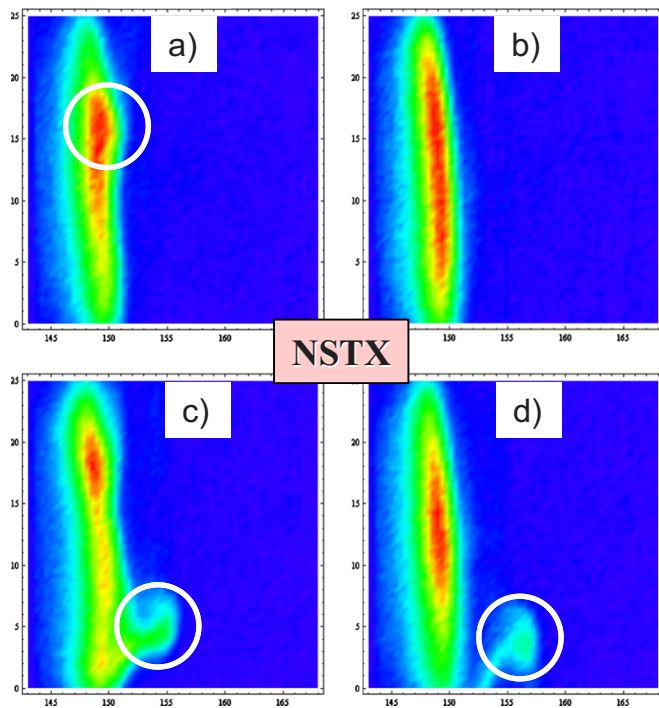
FIG. 9. (Color online) Snapshots from NSTX GPI data for shot 135009. Frame (a) shows a trapped structure (circled) that is never emitted as a blob. Frame (b) is quiescent and typical of most frames. Frames (c) and (d) show a rare blob emission event. The time between frames (c) and (d) is 42 μs.
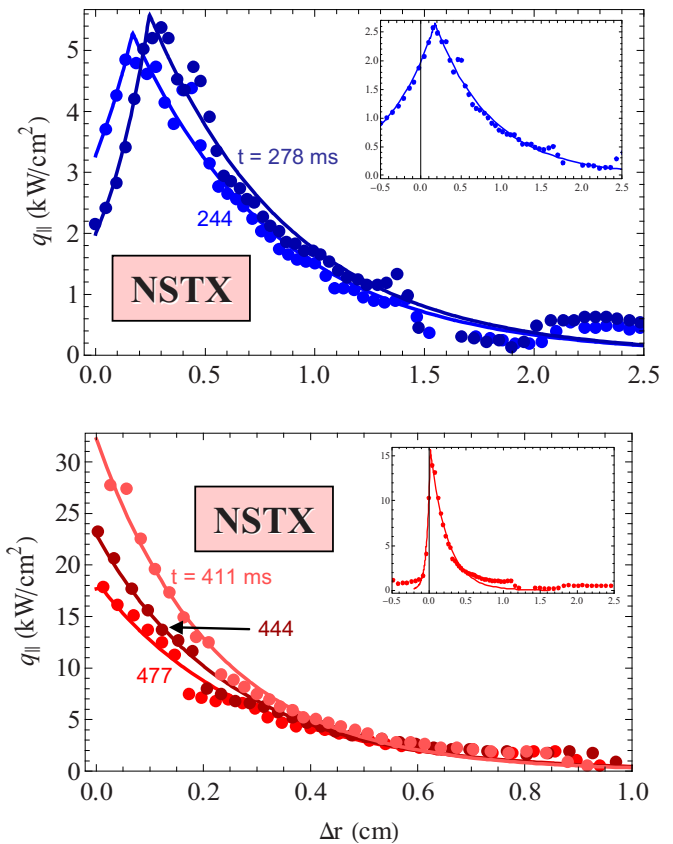

FIG. 10. (Color online) NSTX experimental heat flux, mapped to the outboard midplane for shots 128013 (upper panel, 0.8 MA) and 128797 (lower panel, 1.2 MA). Data from the IRTV at different times are shown as dots, exponential fits are shown as solid lines. Note the difference in x-axis scaling. The insets show the complete profiles, including the private SOL, $\Delta r < 0$, on the same scale.

(Since we do not *a priori* know the "correct" SOL profiles, the system has to find them starting from the initial conditions, and evolving under Eqs. (1)–(4) to establish a turbulent steady-state.) Such a transient event is illustrated in Fig. 8. Frames (a)–(c) show the emission of a blob at successive times. Here, synthetic GPI postprocessing has been applied to the simulation results for comparison with NSTX data (in Fig. 9). Frame (d) shows a typical snapshot late in the simulation after a turbulent quasisteady-state has been established. At these late times, no blobs are released; they are all trapped by the shear layer. This finding is closely related to previous simulation and theory work[38–40] in which it was found that sheared flows strongly suppress the blob transport across the shear layer, either by trapping blobs or tearing them apart.

These simulation results show a strong qualitative connection to the experimental NSTX GPI data. The experiments show intermittent, but very sparse, blob emission in H-mode shots in general, and in shots 135009 and 135038 in particular. Additionally, trapped structures near the separatrix, which propagate down (poloidally) but are not emitted radially, can frequently be seen. Some sample NSTX experimental GPI frames illustrating these points are shown in Fig. 9.

These observations raise the interesting question of identifying the trigger mechanism for blob emission. At present, we do not have a definitive answer, although theoretical mechanisms have been proposed,[41] and experimentally blob emission can be correlated with a local increase in the pressure gradient[37] and may be related to the zonal or mean flow behavior.[14,42,43]

V. SCALING OF THE HEAT-FLUX WIDTH WITH PLASMA CURRENT

A second set of experiments, described in Refs. 4 and 5, was carried out in higher power H-mode discharges ($P_{nb} \approx 6$ MW) on NSTX to determine the scaling of the heat-flux width with plasma current I_p at fixed toroidal field B_t. Experimental results from the IRTV for two cases are shown in Fig. 10, shot 128013 at 0.8 MA and shot 128797 at 1.2 MA. It is evident that the experimental results show a strong scaling with I_p. Two measures of the heat-flux width have been calculated, one from the exponential fits for $\Delta r > 0$, and the other using an integral definition[44] based on Eq. (7),

$$\lambda_{q,\text{int}} = \frac{P_{\text{sep}}}{2\pi R b_\theta q_{\|\text{peak}}}. \tag{10}$$

The resulting widths $\lambda_{q,\text{exp}}$ and $\lambda_{q,\text{int}}$ for the NSTX data are given in Table II.

A companion set of modeling runs using SOLT was obtained and analyzed using a procedure similar to that described in Sec. III, i.e., matching the experimental power by adjusting τ in SOLT. Different values of I_p enter the SOLT simulation inputs through the connection length $L_\|$ as well as through changes in plasma parameters in the respective shots. The results for the heat-flux width versus simulation

TABLE II. Scaling of the SOL width for the I_p current scan. The first five columns, described in the text, are from the NSTX experiment. The last column is the midplane heat-flux width from the SOLT simulations. The ratio of the various quantities for the two shots is also given.

Shot	I_p (MA)	P (MW)	$\lambda_{q,exp}$ (cm)	$\lambda_{q,int}$ (cm)	$\lambda_{q,int,SOLT}$ (cm)
128013	0.8	5.8	0.65	1.73	0.76
128797	1.2	6.1	0.24	0.56	0.58
Ratio	0.67	0.95	2.7	3.1	1.3

FIG. 12. (Color online) Snapshot of the turbulent density fields from SOLT for simulations of shot 128013, I_p=0.8 MA (left) and shot 128797, I_p=1.2 MA (right). The figure shows the separatrix marked by a dashed line. The low I_p case at the left emits blobs while the high I_p case has convective cells trapped near the separatrix and the shear layer.

power P_{sep} are shown in Fig. 11. In this case, the dimensionless parameters for the 128013 run were μ=0.03, β=6.36 $\times 10^{-3}$, and $\alpha_{sheath}=\rho_{sr}/(a_f+b_f \log[x(cm)])$ with a_f=767 cm and b_f=209 cm with reference values T_{er}=99.6 eV, ρ_{sr}=0.48 cm, and b_θ=0.56 (all values quoted at the outboard midplane). The curvature drive parameter β was obtained from Eq. (6) using R at the outboard midplane. For the 128797 run, parameters were μ=0.03, β=6.25$\times 10^{-3}$, a_f=561 cm, b_f=−144 cm, T_{er}=137 eV, ρ_{sr}=0.47 cm, and b_θ=0.69. The simulations for 128797 indicated by an open square and open circle in Fig. 11 employ double the resolution (in both x and y) and double the box size in y, respectively, as a check on numerical convergence. The different connection lengths (a_f and b_f) affect the dynamics of the simulations and, together with the explicit dependence of P_{sep} on b_θ in Eq. (9), result in different slopes in Fig. 11. Simulated heat-flux widths $\lambda_{q,int,SOLT}$ from the straight-line fits for each shot are indicated in Table II.

From Table II it is evident that the simulations, like the experiments, show that λ_q decreases with I_p; however, the scaling in SOLT is much weaker than that in the NSTX experiments. The main mechanism for the heat-flux width in both simulation cases is that discussed in Sec. IV, separatrix-spanning convective cells; however, in the case of shot 128013, some of these convective cells are starting to form
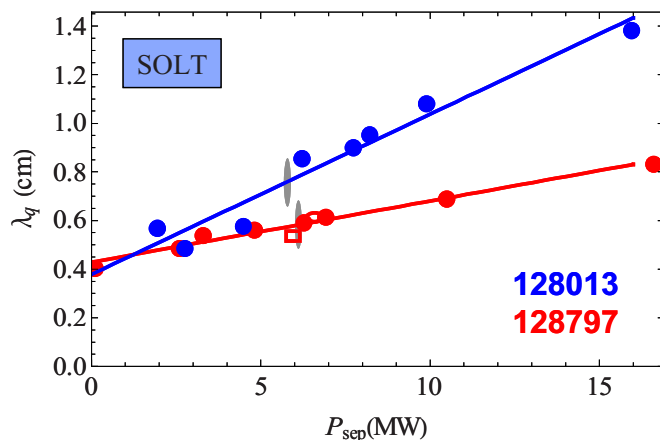

FIG. 11. (Color online) Heat-flux width for simulated power scans for shots 128013 (0.8 MA) and 128797 (1.2 MA). The solid lines are linear fits. Thin gray ellipses mark the actual experimental power levels for these two shots. The open symbols near 6 MW for shot 128797 are convergence study runs. Reprinted from Ref. 24, J. R. Myra, D. A. Russell, D. A. D'Ippolito, J.-W. Ahn, R. Maingi, R. J. Maqueda, D. P. Lundberg, D. P. Stotler, S. J. Zweben, and M. Umansky, J. Nucl. Mater. (in press), with permission from Elsevier.
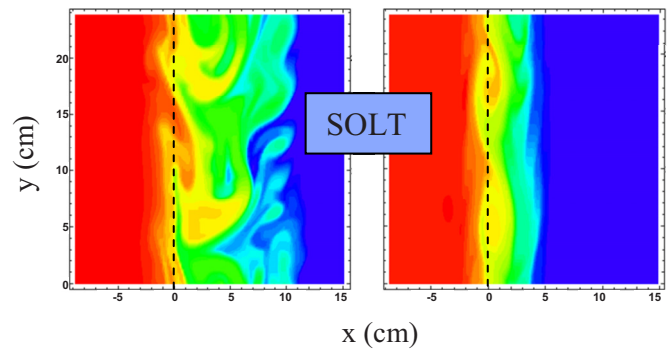
structures which break free as large blobs. In SOLT the decreased heat-flux width at the larger I_p of shot 128797 can be attributed primarily to a small reduction in turbulent activity at shorter connection length due to stronger sheath conductivity. Snapshots of the turbulence for the two simulation runs that best match the experiments are shown in Fig. 12. Although these visual images of the turbulence look quite different for the two cases, because the lower I_p case exceeds the threshold for spontaneous blob emission, the turbulence and transport levels in the region close to the separatrix (i.e., within a few λ_q) are too similar to yield a strong I_p scaling of λ_q as observed in the experiments. Figure 12(b) illustrates the same type of separatrix-spanning convective cells seen in Figs. 7 and 8(d).

While the absolute level of agreement in Table II between SOLT and NSTX is approximately a factor of 2 (and hence within the absolute accuracy expected of the modeling), the scaling with I_p is clearly different. Two hypotheses can be put forward to explain this discrepancy of heat flux scaling widths: (i) the SOLT model for midplane turbulence does not correctly reflect midplane turbulence and transport levels in NSTX, or (ii) physics other than midplane turbulence (e.g., cross-field transport between the X-point and the divertor plate) is responsible for additional broadening of λ_q at low I_p. We now show that (i) can likely be ruled out.

To test (i) we carried out a direct comparison of midplane turbulence between NSTX data and SOLT using the midplane GPI diagnostic and its synthetic counterpart in SOLT. Results are shown in Fig. 13. In the figure, the similar shot 128808 has been used as a substitute for 128797 because of lack of good NSTX GPI data for 128797. Only the region $0 < x < 4$ cm in the figure is relevant to the near-SOL heat-flux width. In this region, both NSTX data and SOLT simulations show that the midplane turbulence levels, as characterized by $\delta I_{rms}/\langle I \rangle$, are similar for the two shots. Both NSTX and SOLT show slightly lower levels for shot 128979, but the difference is not large enough to account for a factor of 3 in λ_q. The skewness of the fluctuations versus radius (not shown) for the two shots is also similar in both NSTX and SOLT. Thus, we conclude from the available data that the SOLT model is providing a reasonably faithful descrip-
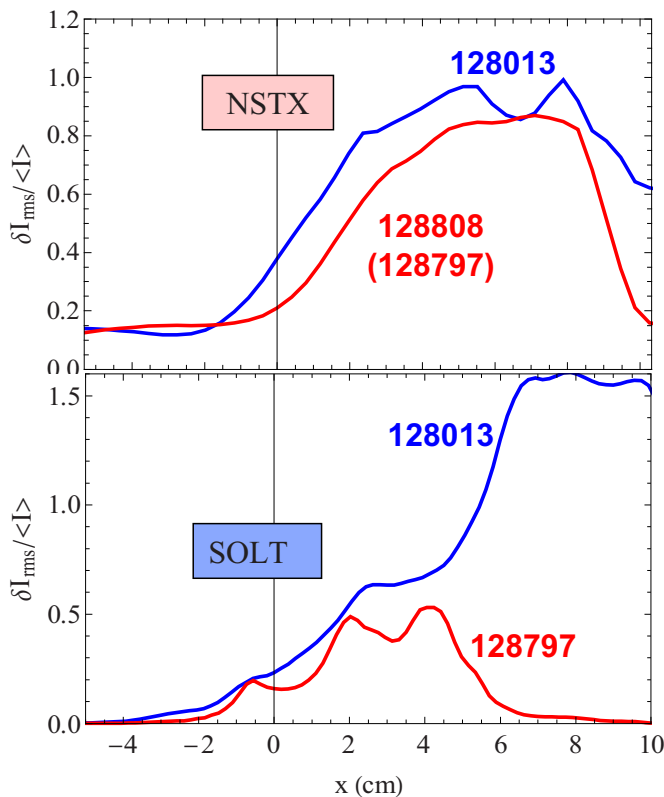
FIG. 13. (Color online) Radial structure of the normalized GPI fluctuation level $\delta I_{rms}/\langle I \rangle$ for NSTX data (upper) and SOLT synthetic GPI (lower). Only the region $x < 4$ cm is relevant to the heat-flux width.

tion of the midplane turbulence and that turbulence does not have a strong dependence on I_p. The explanation for the strong variation of the heat-flux width measured at the divertor must lie elsewhere.

We note parenthetically that there is a discrepancy between NSTX and SOLT in the far SOL fluctuation level for shot 128797. In this case, as discussed in connection with Fig. 12, the simulations were below the threshold for blob emission causing $\delta I_{rms}/\langle I \rangle$ to drop to zero in the far SOL.

The comparison in Fig. 13 therefore suggests hypothesis (ii), physics other than midplane turbulence is responsible for strong broadening of λ_q in the low I_p discharge. Some possibilities are large ion orbit excursions and ion X-point loss at low I_p,[45] differences in downstream sheath conditions at the plates in the two cases, ELM and magneto-hydrodynamic effects which could cause strike point motion,[46] and divertor leg instabilities.[47] Exploration of these possibilities remains for other investigations.

VI. DISCUSSION AND CONCLUSIONS

In this paper, we have employed the 2D electrostatic fluid turbulence code SOLT to calculate midplane SOL plasma profiles and heat-flux widths. The most important inputs to our model, which distinguish the modeling of one shot from another, are the power crossing the separatrix P_{sep}, $L_\parallel/R$ which gives the ratio of connection length (sheath dissipation) to major radius (curvature drive), and the plasma profiles inside the LCFS which provide free energy from

their gradients and dictate the collisionality regime. Simulations in this paper are essentially in the sheath-connected regime.

We carried out two sets of SOLT simulations and compared the results with NSTX data. In the first set, for low power ELM-free H-modes, we obtained a weak scaling of the heat-flux width λ_q with power, in agreement with experimental data. Furthermore, the rough absolute size of λ_q obtained by the simulations was similar to the measured value. The physics of midplane turbulence in the SOLT simulations was validated by direct comparison of calculated midplane density and temperature profiles with reciprocating probe data. We conclude that for these shots midplane-region electrostatic turbulence is the main contributor to the heat-flux width.

In the second set of simulations, for higher power discharges, we examined the dependence of λ_q on plasma current I_p (at fixed B_t). Although a strong dependence was observed in the NSTX heat-flux width measured experimentally at the divertor plates, in the SOLT simulations the dependence was much weaker (but in the same direction— larger λ_q for small I_p). We confirmed that the level of midplane turbulence was not a strong function of I_p in either the SOLT simulations or the NSTX data by using a synthetic GPI diagnostic for the comparison. Thus, we conclude that mechanisms other than midplane electrostatic turbulence must be responsible for at least some of the strong I_p scaling observed in the experiments.

For comparison of these results with earlier studies, we note that experimental scalings of λ_q were also obtained in a previous work for the Mega Ampere Spherical Tokamak (MAST) (Ref. 10) although under somewhat different conditions: L-mode double-null plasmas in the parallel conduction-limited regime. In this case, the authors obtained a weak negative scaling with P_{sep} and a strong positive scaling with $L_\parallel \propto 1/I_p$. Results were compared with analytical scalings from local transport models. The best fit was obtained for a scaling based on perpendicular transport driven by resistive interchange modes. The observed $L_\parallel$ scaling was stronger than that predicted by the local transport model. Thus, the conclusions from that study are similar to what we find here in several respects. First, the underlying turbulence simulated by SOLT is of the interchange type. Second, the conclusions regarding $L_\parallel$ or I_p scalings seem qualitatively similar. Finally, both studies find a weak P_{sep} scaling, although in Ref. 10 the power scaling is negative, compared with positive here. This difference is likely due to the difference between sheath-limited and condition-limited parallel transport (see Appendix A). Heavy lithium coating on the plasma-facing components in NSTX has led to lower recycling condition in the divertor plasma and many perpendicular transport models in Ref. 9 indeed produce positive power scaling in the collisionless regime.

From SOLT simulations, we find that intermittent separatrix-spanning convective cells are the cross-field transport mechanism that dominates the near-SOL width for NSTX H-mode plasmas. This may be the most important physics result of the present paper. The convective cells occur as a result of interchange turbulence. The wave crests

TABLE III. Coefficients for the fit given by Eq. (B2).

Domain	A	B	C
1	2.62×10^{12}	-5.28×10^2	5.39×10^{12}
2	3.41×10^{12}	-7.31×10^2	8.08×10^{12}
3	4.30×10^{12}	-9.81×10^2	1.16×10^{13}
4	5.47×10^{12}	-1.33×10^3	1.67×10^{13}
5	6.72×10^{12}	-1.74×10^3	2.56×10^{13}
6	7.36×10^{12}	-2.00×10^3	3.35×10^{13}
7	8.54×10^{12}	-2.32×10^3	3.94×10^{13}
8	9.92×10^{12}	-2.15×10^2	2.99×10^{13}
9	1.90×10^{13}	-3.36×10^3	4.77×10^{12}
10	2.93×10^{13}	-4.41×10^3	-2.08×10^{13}
11	4.25×10^{13}	-6.49×10^3	-3.51×10^{13}
12	5.06×10^{13}	-9.13×10^3	-3.37×10^{13}
13	5.15×10^{13}	-9.59×10^3	-2.48×10^{13}
14	6.35×10^{13}	-3.47×10^3	-5.07×10^{13}
15	7.19×10^{13}	-1.97×10^2	-6.68×10^{13}
16	7.98×10^{13}	5.44×10^3	-8.42×10^{13}

FIG. 14. (Color online) Test case comparison of the DEGAS 2 neutral puff profile with the smoothed fit.

bulge out from the strong gradient region into the SOL, and are sheared by the strong mean flows present in H-mode discharges. The strong shearing prevents these objects from being emitted as blobs, but they contribute to transport and the near-SOL width because they carry plasma onto the open field lines where it can be lost. Evidence for poloidally propagating trapped structures is sometimes seen in the NSTX GPI data for H-mode discharges.

Finally, as an interesting side-note to the main subject of the present paper, we found that blob emission in H-mode simulations could be triggered by transient events, such as at the start of a simulation. In most cases, the simulations then settled down to a quasisteady-state in which there was no blob emission. Rather, nascent blobs in SOLT were trapped by the strong sheared flows. NSTX GPI data show that blob emission in H-mode is rare and some evidence for trapped blobs was found. (In rough order of magnitude, the waiting time between blob emissions from a 2 ms sample of GPI data, covering a camera view of about 25 cm poloidally, was about 300 μs, which is to be compared with a typical blob lifetime of 20–30 μs.) This raises the possibility that when rare blob emission occurs, it could be triggered by transient events, perhaps propagating outward from the core. The subject of blob triggering remains an interesting topic for future work.

ACKNOWLEDGMENTS

APPENDIX A: PARALLEL CLOSURES

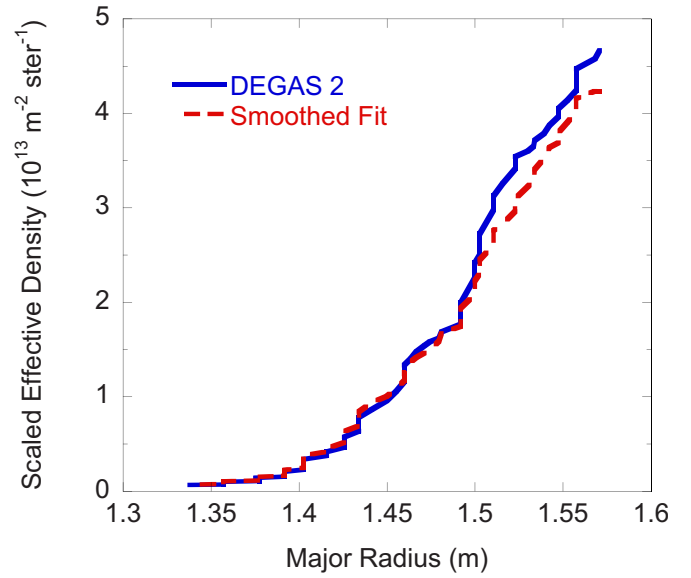In this appendix, we give closure relations for the parallel heat flux and parallel current that apply to both the sheath-limited (SL) and conduction-limited (CL) regimes. A flux limit (FL) is also imposed to ensure that the fluxes do not exceed physically meaningful values under any circumstances (e.g., which may arise due to transients in the simulation).

The dimensionless forms of the parallel heat flux in the various regimes are[48–50]

$$q_{\parallel SL} = s_E n T^{3/2} e^{(\Phi_B - \Phi)/T}, \tag{A1}$$

$$q_{\parallel FL} = C_{fle} n T^{3/2}, \tag{A2}$$

$$q_{\parallel CL} = \frac{3.2 n T^{3/2}}{\Lambda} = \frac{3.2 T^{7/2}}{\Lambda_r} \frac{\alpha_{sh}}{\alpha_{sh0}}, \tag{A3}$$

where α_{sh0} is the value of α_{sh} at a reference value of connection length $L_{\parallel}$ and the dimensionless collisionality parameter is given by

$$\Lambda = \frac{\nu_{ei} L_{\parallel}}{\Omega_e \rho_s}. \tag{A4}$$

The SOL electron collisionality parameter ν_{*e} introduced by some authors is just $\nu_{*e} = L_{\parallel}/\lambda_{ei} = \Lambda (m_i/m_e)^{1/2}$, where λ_{ei} is the electron mean free path for collisions with ions. The flux limit for electron heat conduction is $C_{fle} = 60 \sim (m_i/m_e)^{1/2}$. A smooth interpolation between regimes is given by

$$1/q_{\parallel} = 1/q_{\parallel SL} + 1/q_{\parallel FL} + 1/q_{\parallel CL}, \tag{A5}$$

so effectively the smallest $q_{\parallel}$ dominates the result. As collisionality is raised, the system transitions from sheath-limited to conduction-limited.

For the parallel current, a similar philosophy (i.e., piecing together asymptotic results from the different regimes) is employed, with

$$J_{\parallel SL} = n T^{1/2} (1 - e^{(\Phi_B - \Phi)/T}), \tag{A6}$$

$$J_{\parallel eFL} = -C_{fle} n T^{1/2}, \tag{A7}$$

$$J_{\parallel CL} = 1.96 \frac{T^{2.5}}{\Lambda_r} \frac{(\Phi - \Phi_B)}{T} \frac{\alpha_{sh}}{\alpha_{sh0}}. \tag{A8}$$

Here, and for the heat flux, we regard Φ_B as a free order-unity parameter, which is ≈ 3 for isothermal sheaths in a D plasma, 1.71 for conduction-limited fluxes, and perhaps smaller yet to account for cold divertor plates. In the sheath-limited regime, Eq. (A6) applies. For large positive Φ, this function automatically yields the ion saturation current. For large negative Φ, where the electron saturation current is the physical result, Eq. (A7) applies. Finally, for large Λ, the collisional regime, Eq. (A8), applies. The interpolation between regimes is given by

$$1/J_\parallel = 1/J_{\parallel SL} + \Theta(\Phi_B - \Phi)/J_{\parallel eFL} + 1/J_{\parallel CL}, \tag{A9}$$

where $\Theta(\Phi_B - \Phi)$ is the Heaviside step function.

APPENDIX B: NEUTRAL PUFF PROFILE FOR SYNTHETIC GPI

Simulating the turbulence imaged by the GPI diagnostic requires knowledge of the puffed neutral density profile for the principle emitting state, n_0. The profile of n_0 results from the migration of neutrals from the GPI gas manifold into the plasma, dependent on the rates of dissociation, ionization, and charge exchange, which in turn depend on the plasma density and temperature. For the relatively low densities of the GPI puff, neutral-neutral collisions can be ignored. n_0 is then completely determined by the plasma n_e and T_e profiles, which vary from shot to shot within a limited range. The Monte Carlo code DEGAS 2 can be used to accurately simulate neutral density profiles from the GPI manifold. The three-dimensional function n_0 produced by DEGAS 2 is converted to an "effective density" $n_{0,eff}$ by calculating the line-integrated neutral density projected onto the GPI camera view. Combined with the atomic physics function F and the GPI target plane n_e and T_e, the effective density is used to calculate the synthetic GPI camera image,

$$I(i) = F[n_e(i), T_e(i)] n_{0,eff}(i), \tag{B1}$$

where i indexes the spatial domains, as described subsequently.

Initial GPI experiments and the associated DEGAS 2 simulations used helium.[27] Because this work is concerned with deuterium GPI, a number of the original DEGAS 2 GPI simulations were run again with deuterium, and a method to provide the atomic deuterium density profile in the GPI camera view for arbitrary NSTX-relevant n_e and T_e profiles was developed. The D_2 simulations included two NSTX L-mode shots, 112814 and 112825, and one NSTX H-mode shot, 112811. To expand the parameter space and isolate the individual contributions of n_e and T_e, four additional artificial shots were produced by linearly scaling the 112814 n_e by 0.5 and 1.2, and the 112814 T_e by 0.67 and 2.

The GPI camera view is 64×64 pixels. Only the radial variation is of interest, so the 32nd row of the image is used. Each 64 pixel profile is decomposed into 16 domains of four pixels each, with domain 1 closest to the core, and domain 16 closest to the edge. Using all seven profiles, each domain is individually fit with a multiple linear regression solver,

mvregress.m in the MATLAB statistics package. The fit is of the form

$$n_{fit,i} = A_i + B_i(n_{e,i})^{1/2} + C_i(T_{e,i})^{-1/2}, \tag{B2}$$

where n_e and T_e are the values mapped to the GPI target plane in m^{-3} and eV, respectively. A_i, B_i, and C_i are constants for each of the 16 domains. The values of the exponents and coefficients were determined by minimizing the summed residual of the fit,

$$R_{tot} = \frac{\Sigma_i |n_{0,i} - n_{fit,i}|}{\Sigma_i |n_{0,i}|}. \tag{B3}$$

This error criterion was chosen to give a greater weight to the values close to the edge, as a larger relative error near the core is less consequential for the GPI simulations. The typical single-point accuracy of the fit is within 10% of the profiles computed by the DEGAS 2 code. The fits are valid within the parameter space range covered by the seven input profiles (n_e and T_e). The fit coefficients are given in Table III. A source flux of 1×10^{20} m^{-2} s^{-1} is assumed, but the fit coefficients can be linearly scaled. To reduce artificial discontinuities, a four-point moving average is applied to smooth the resulting profiles prior to use in simulations. As an example, Fig. 14 contains the n_0 profile for NSTX shot 112814 as computed by DEGAS 2 and the method above in m^{-2} sr^{-1}.

[1]B. Lipschultz, X. Bonnin, G. Counsell, A. Kallenbach, A. Kukushkin, K. Krieger, A. Leonard, A. Loarte, R. Neu, R. A. Pitts, T. Rognlien, J. Roth, C. Skinner, J. L. Terry, E. Tsitrone, D. Whyte, S. Zweben, N. Asakura, D. Coster, R. Doerner, R. Dux, G. Federici, M. Fenstermacher, W. Fundamenski, P. Ghendrih, A. Herrmann, J. Hu, S. Krasheninnikov, G. Kirnev, A. Kreter, V. Kurnaev, B. LaBombard, S. Lisgo, T. Nakano, N. Ohno, H. D. Pacher, J. Paley, Y. Pan, G. Pautasso, V. Philipps, V. Rohde, D. Rudakov, P. Stangeby, S. Takamura, T. Tanabe, Y. Yang, and S. Zhu, Nucl. Fusion **47**, 1189 (2007).

[2]C. J. Lasnier, M. A. Makowski, J. A. Boedo, S. L. Allen, N. H. Brooks, D. N. Hill, A. W. Leonard, J. G. Watkins, and W. P. West, "Scaling of divertor heat flux profile widths in DIII-D," J. Nucl. Mater. (in press).

[3]B. LaBombard, J. L. Terry, J. W. Hughes, D. Brunner, J. Payne, M. L. Reinke, Y. Lin, and S. Wukitch, "Divertor heat flux footprints in EDA H-mode discharges on Alcator C-Mod," J. Nucl. Mater. (in press).

[4]T. K. Gray, R. Maingi, V. A. Soukhanovskii, J. E. Surany, J.-W. Ahn, and A. G. McLean, "Dependence of divertor heat flux widths on heating power, flux expansion, and plasma current in the NSTX," J. Nucl. Mater. (submitted).

[5]R. Maingi, C. E. Bush, R. Kaita, H. W. Kugel, A. L. Roquemore, S. F. Paul, V. A. Soukhanovskii, and NSTX Team, J. Nucl. Mater. **363–365**, 196 (2007).

[6]J. W. Ahn (private communication), 2010.

[7]S.-I. Itoh and K. Itoh, Plasma Phys. Controlled Fusion **36**, 1845 (1994).

[8]G. F. Counsell, J. W. Connor, S. K. Erents, A. R. Field, S. J. Fielding, B. La Bombard, and K. M. Morel, J. Nucl. Mater. **266–269**, 91 (1999).

[9]J. W. Connor, G. F. Counsell, S. K. Erents, S. J. Fielding, B. LaBombard, and K. Morel, Nucl. Fusion **39**, 169 (1999).

[10]J.-W. Ahn, G. F. Counsell, and A. Kirk, Plasma Phys. Controlled Fusion **48**, 1077 (2006).

[11]W. Fundamenski, O. E. Garcia, V. Naulin, R. A. Pitts, A. H. Nielsen, J. Juul Rasmussen, J. Horacek, J. P. Graves, and JET EFDA Contributors, Nucl. Fusion **47**, 417 (2007).

[12]S. I. Krasheninnikov, D. A. D'Ippolito, and J. R. Myra, J. Plasma Phys. **74**, 679 (2008).

[13]S. J. Zweben, J. L. Terry, B. LaBombard, M. Agostini, M. Greenwald, O. Grulke, J. W. Hughes, D. A. D'Ippolito, S. I. Krasheninnikov, J. R. Myra, D. A. Russell, D. P. Stotler, and M. Umansky, "Estimate of convective radial transport due to SOL turbulence as measured by GPI in Alcator C-Mod," J. Nucl. Mater. (in press).

14 D. A. Russell, J. R. Myra, and D. A. D'Ippolito, Phys. Plasmas **16**, 122304 (2009) and references therein.

15 S. M. Kaye, M. G. Bell, R. E. Bell, J. Bialek, T. Bigelow, M. Bitter, P. Bonoli, D. Darrow, P. Efthimion, J. Ferron, E. Fredrickson, D. Gates, L. Grisham, J. Hosea, D. Johnson, R. Kaita, S. Kubota, H. Kugel, B. LeBlanc, R. Maingi, J. Manickam, T. K. Mau, R. J. Maqueda, E. Mazzucato, J. Menard, D. Mueller, B. Nelson, N. Nishino, M. Ono, F. Paoletti, S. Paul, Y.-K. M. Peng, C. K. Phillips, R. Raman, P. Ryan, S. A. Sabbagh, M. Schaffer, C. H. Skinner, D. Stutman, D. Swain, E. Synakowski, Y. Takase, J. Wilgen, J. R. Wilson, W. Zhu, S. Zweben, A. Bers, M. Carter, B. Deng, C. Domier, E. Doyle, M. Finkenthal, K. Hill, T. Jarboe, S. Jardin, H. Ji, L. Lao, K. C. Lee, N. Luhmann, R. Majeski, S. Medley, H. Park, T. Peebles, R. I. Pinsker, G. Porter, A. Ram, M. Rensink, T. Rognlien, D. Stotler, B. Stratton, G. Taylor, W. Wampler, G. A. Wurden, X. Q. Xu, and L. Zeng, Phys. Plasmas **8**, 1977 (2001).

16 J. R. Myra, D. A. D'Ippolito, D. P. Stotler, S. J. Zweben, B. P. LeBlanc, J. E. Menard, R. J. Maqueda, and J. Boedo, Phys. Plasmas **13**, 092509 (2006).

17 D. A. D'Ippolito, J. Boedo, D. P. Lundberg, R. Maqueda, J. R. Myra, D. A. Russell, D. P. Stotler, and S. J. Zweben, *Proceedings of the 22nd Fusion Energy Conference*, Geneva, 2008 (IAEA, Vienna, 2009).

18 D. A. Russell, J. R. Myra, D. A. D'Ippolito, T. L. Munsat, Y. Sechrest, R. J. Maqueda, D. P. Stotler, S. J. Zweben, and NSTX Team, "Comparison of scrape-off layer turbulence simulations with experiments using a synthetic gas puff imaging diagnostic," Phys. Plasmas (submitted).

19 O. E. Garcia, J. Horacek, R. A. Pitts, A. H. Nielsen, W. Fundamenski, V. Naulin, and J. Juul Rasmussen, Nucl. Fusion **47**, 667 (2007).

20 O. E. Garcia, Plasma Fusion Res. **4**, 019 (2009).

21 Y. Sarazin, Ph. Ghendrih, G. Attuel, C. Clément, X. Garbet, V. Grandgirard, M. Ottaviani, S. Benkadda, P. Beyer, N. Bian, and C. Figarella, J. Nucl. Mater. **313–316**, 796 (2003).

22 Ph. Ghendrih, P. Kaw, Y. Sarazin, P. Beyer, S. Benkadda, G. Falchetto, X. Garbet, V. Grandgirard, and M. Ottaviani, *Proceedings of the 20th Fusion Energy Conference*, Vilamoura, 2004 (IAEA, Vienna, 2005).

23 P. Ricci and B. N. Rogers, Phys. Plasmas **16**, 062303 (2009).

24 J. R. Myra, D. A. Russell, D. A. D'Ippolito, J.-W. Ahn, R. Maingi, R. J. Maqueda, D. P. Lundberg, D. P. Stotler, S. J. Zweben, and M. Umansky, "Turbulent transport and the scrape-off-layer width," J. Nucl. Mater. (in press).

25 S. J. Zweben, R. J. Maqueda, D. P. Stotler, A. Keesee, J. Boedo, C. E. Bush, S. M. Kaye, B. LeBlanc, J. L. Lowrance, V. J. Mastrocola, R. Maingi, N. Nishino, G. Renda, D. W. Swain, J. B. Wilgen, and NSTX Team, Nucl. Fusion **44**, 134 (2004).

26 R. J. Maqueda, G. A. Wurden, D. P. Stotler, S. J. Zweben, B. LaBombard, J. L. Terry, J. L. Lowrance, V. J. Mastrocola, G. F. Renda, D. A. D'Ippolito, J. R. Myra, and N. Nishino, Rev. Sci. Instrum. **74**, 2020 (2003).

27 D. P. Stotler, J. Boedo, B. LeBlanc, R. J. Maqueda, and S. J. Zweben, J. Nucl. Mater. **363–365**, 686 (2007).

28 J. R. Myra, D. A. Russell, and D. A. D'Ippolito, Phys. Plasmas **15**, 032304 (2008).

29 K. C. Shaing and E. C. Crume, Jr., Phys. Rev. Lett. **63**, 2369 (1989).

30 K. H. Burrell, Phys. Plasmas **4**, 1499 (1997).

31 P. W. Terry, Rev. Mod. Phys. **72**, 109 (2000).

32 P. H. Diamond, S.-I. Itoh, K. Itoh, and T. S. Hahm, Plasma Phys. Controlled Fusion **47**, R35 (2005).

33 R. M. McDermott, B. Lipschultz, J. W. Hughes, P. J. Catto, A. E. Hubbard, I. H. Hutchinson, R. S. Granetz, M. Greenwald, B. LaBombard, K. Marr, M. L. Reinke, J. E. Rice, D. Whyte, and Alcator C-Mod Team, Phys. Plasmas **16**, 056103 (2009).

34 R. J. Goldston, Phys. Plasmas **17**, 012503 (2010).

35 J. A. Boedo, N. Crocker, L. Chousal, R. Hernandez, J. Chalfant, H. Kugel, P. Roney, J. Wertenbaker, and NSTX Team, Rev. Sci. Instrum. **80**, 123506 (2009).

36 N. Bisai, A. Das, S. Deshpande, R. Jha, P. Kaw, A. Sen, and R. Singh, Phys. Plasmas **12**, 072520 (2005).

37 I. Furno, B. Labit, A. Fasoli, F. M. Poli, P. Ricci, C. Theiler, S. Brunner, A. Diallo, J. P. Graves, M. Podestà, and S. H. Müller, Phys. Plasmas **15**, 055903 (2008).

38 Ph. Ghendrih, Y. Sarazin, G. Attuel, S. Benkadda, P. Beyer, G. Falchetto, C. Figarella, X. Garbet, V. Grandgirard, and M. Ottaviani, Nucl. Fusion **43**, 1013 (2003).

39 G. Q. Yu and S. I. Krasheninnikov, Phys. Plasmas **10**, 4413 (2003).

40 J. R. Myra, D. A. D'Ippolito, S. I. Krasheninnikov, and G. Q. Yu, Phys. Plasmas **11**, 4267 (2004).

41 S. I. Krasheninnikov and A. I. Smolyakov, Phys. Plasmas **14**, 102503 (2007).

42 S. J. Zweben, R. J. Maqueda, R. Hager, K. Hallatschek, S. Kaye, T. Munsat, F. M. Poli, L. Roquemore, Y. Sechrest, and D. P. Stotler, Phys. Plasmas **17**, 102502 (2010).

43 M. Agostini, S. J. Zweben, R. Cavazzana, P. Scarin, G. Serianni, R. J. Maqueda, and D. P. Stotler, Phys. Plasmas **14**, 102305 (2007).

44 A. Loarte, S. Bosch, A. Chankin, S. Clement, A. Herrmann, D. Hill, K. Itami, J. Lingertat, B. Lipschultz, K. McCormick, R. Monk, G. D. Porter, M. Shimada, and M. Sugihara, J. Nucl. Mater. **266–269**, 587 (1999).

45 S. Ku, H. Baek, and C. S. Chang, Phys. Plasmas **11**, 5626 (2004).

46 E. R. Solano, S. Jachmich, F. Villone, N. Hawkes, Y. Corre, R. A. Pitts, A. Loarte, B. Alper, K. Guenther, A. Koroktov, M. Stamp, P. Andrew, S. A. Arshad, J. Conboy, T. Bolzonella, E. Rachlew, M. Kempenaars, A. Cenedese, D. Testa, and JET EFDA Contributors, J. Nucl. Mater. **337–339**, 747 (2005).

47 D. D. Ryutov and R. H. Cohen, Contrib. Plasma Phys. **48**, 48 (2008).

48 S. I. Braginskii, *Reviews of Plasma Physics* (Consultants Bureau, New York, 1965), Vol. 1.

49 P. C. Stangeby, *The Plasma Boundary of Magnetic Fusion Devices* (IOP, Bristol, 2000).

50 J. D. Huba, *NRL Plasma Formulary* (Naval Research Laboratory, Washington, 2009).